Biomedical Optics EXPRESS

Toward *in vivo* biopsy of melanoma based on photoacoustic and ultrasound dual imaging with an integrated detector

Yating Wang,[1,2] Dong Xu,[1,2] Sihua Yang,[1,3] and Da Xing[1,*]

[1]*MOE Key Laboratory of Laser Life Science & Institute of Laser Life Science, College of Biophotonics, South China Normal University, Guangzhou 510631, China*
[2]*These authors contributed equally to this work*
[3]*yangsh@scnu.edu.cn*
[*]*xingda@scnu.edu.cn*

Abstract: Melanoma is the most dangerous type of skin cancer with high lethal rate. Tumor thickness and tumor-associated vasculature are two key parameters for staging melanoma. Previous techniques for diagnosing melanoma have insurmountable restrictions, such as invasive, low specificity, or inaccurate depth measurement. Here we develop an integrated photoacoustic (PA) and ultrasound (US) imaging system dedicated to overcome these limitations. An integrated detector with sound-light coaxial/confocal design and flexible coupling mode is employed for the combined PA/US imaging strategy. PA imaging results enable a clear characterization of tumor angiogenesis with high resolution and high contrast. Furthermore, accurate thickness measurements of melanoma in different stages can be resolved with the simultaneously obtained PA/US image. Phantom experiments and *in vivo* animal experimental results demonstrate the integrated PA/US system could provide potential for noninvasive biopsy of melanoma.

OCIS codes: (170.3880) Medical and biological imaging; (110.5120) Photoacoustic imaging; (170.0180) Microscopy.

References and links

1. A. J. Miller and M. C. Mihm, Jr., "Melanoma," N. Engl. J. Med. **355**(1), 51–65 (2006).
2. E. M. Dunki-Jacobs, G. G. Callender, and K. M. McMasters, "Current management of melanoma," Curr. Probl. Surg. **50**(8), 351–382 (2013).
3. A. Srivastava, R. Ralhan, and J. Kaur, "Angiogenesis in cutaneous melanoma: pathogenesis and clinical implications," Microsc. Res. Tech. **60**(2), 208–224 (2003).
4. S. C. Shivers, X. Wang, W. Li, E. Joseph, J. Messina, L. F. Glass, R. DeConti, C. W. Cruse, C. Berman, N. A. Fenske, G. H. Lyman, and D. S. Reintgen, "Molecular staging of malignant melanoma: correlation with clinical outcome," JAMA **280**(16), 1410–1415 (1998).
5. W. H. Clark, Jr., A. M. Ainsworth, E. A. Bernardino, C. H. Yang, C. M. Mihm, Jr., and R. J. Reed, "The developmental biology of primary human malignant melanomas," Semin. Oncol. **2**(2), 83–103 (1975).
6. C. M. Balch, J. E. Gershenwald, S. J. Soong, J. F. Thompson, M. B. Atkins, D. R. Byrd, A. C. Buzaid, A. J. Cochran, D. G. Coit, S. Ding, A. M. Eggermont, K. T. Flaherty, P. A. Gimotty, J. M. Kirkwood, K. M. McMasters, M. C. Mihm, Jr., D. L. Morton, M. I. Ross, A. J. Sober, and V. K. Sondak, "Final version of 2009 AJCC melanoma staging and classification," J. Clin. Oncol. **27**(36), 6199–6206 (2009).
7. N. Cascinelli, "Margin of resection in the management of primary melanoma," Semin. Surg. Oncol. **14**(4), 272–275 (1998).
8. J. Cook, "Surgical margins for resection of primary cutaneous melanoma," Clin. Dermatol. **22**(3), 228–233 (2004).
9. L. Nie and X. Chen, "Structural and functional photoacoustic molecular tomography aided by emerging contrast agents," Chem. Soc. Rev. **43**(20), 7132–7170 (2014).
10. N. Lassau, M. Lamuraglia, S. Koscielny, A. Spatz, A. Roche, J. Leclere, and M. F. Avril, "Prognostic value of angiogenesis evaluated with high-frequency and colour Doppler sonography for preoperative assessment of primary cutaneous melanomas: correlation with recurrence after a 5 year follow-up period," Cancer Imaging **6**(1),

#253727 Received 12 Nov 2015; revised 14 Dec 2015; accepted 15 Dec 2015; published 5 Jan 2016

24–29 (2006).
11. C. Benvenuto-Andrade, S. W. Dusza, A. L. C. Agero, A. Scope, M. Rajadhyaksha, A. C. Halpern, and A. A. Marghoob, "Differences between polarized light dermoscopy and immersion contact dermoscopy for the evaluation of skin lesions," Arch. Dermatol. **143**(3), 329–338 (2007).
12. X. Wortsman, "Ultrasound in dermatology: why, how, and when?" Semin. Ultrasound CT MR **34**(3), 177–195 (2013).
13. M. Scotto di Santolo, M. Sagnelli, M. Mancini, M. Scalvenzi, M. Delfino, F. Schonauer, G. Molea, F. Ayala, and M. Salvatore, "High-resolution color-Doppler ultrasound for the study of skin growths," Arch. Dermatol. Res. **307**(7), 559–566 (2015).
14. G. Pellacani, A. M. Cesinaro, and S. Seidenari, "Reflectance-mode confocal microscopy of pigmented skin lesions--improvement in melanoma diagnostic specificity," J. Am. Acad. Dermatol. **53**(6), 979–985 (2005).
15. W. Dummer, H. J. Blaheta, B. C. Bastian, T. Schenk, E. V. Bröcker, and W. Remy, "Preoperative characterization of pigmented skin lesions by epiluminescence microscopy and high-frequency ultrasound," Arch. Dermatol. **131**(3), 279–285 (1995).
16. J. L. Semple, A. K. Gupta, L. From, K. A. Harasiewicz, D. N. Sauder, F. S. Foster, and D. H. Turnbull, "Does high-frequency (40-60 MHz) ultrasound imaging play a role in the clinical management of cutaneous melanoma?" Ann. Plast. Surg. **34**(6), 599–606 (1995).
17. S. M. Swetter, "Dermatological perspectives of malignant melanoma," Surg. Clin. North Am. **83**(1), 77–95 (2003).
18. W. Song, W. Zheng, R. Liu, R. Lin, H. Huang, X. Gong, S. Yang, R. Zhang, and L. Song, "Reflection-mode in vivo photoacoustic microscopy with subwavelength lateral resolution," Biomed. Opt. Express **5**(12), 4235–4241 (2014).
19. G. He, D. Xu, H. Qin, S. Yang, and D. Xing, "In vivo cell characteristic extraction and identification by photoacoustic flow cytography," Biomed. Opt. Express **6**(10), 3748–3756 (2015).
20. L. V. Wang and S. Hu, "Photoacoustic tomography: in vivo imaging from organelles to organs," Science **335**(6075), 1458–1462 (2012).
21. Z. Chen, S. Yang, and D. Xing, "In vivo detection of hemoglobin oxygen saturation and carboxyhemoglobin saturation with multiwavelength photoacoustic microscopy," Opt. Lett. **37**(16), 3414–3416 (2012).
22. K. Peng, L. He, B. Wang, and J. Xiao, "Detection of cervical cancer based on photoacoustic imaging-the in-vitro results," Biomed. Opt. Express **6**(1), 135–143 (2015).
23. X. Ji, K. Xiong, S. Yang, and D. Xing, "Intravascular confocal photoacoustic endoscope with dual-element ultrasonic transducer," Opt. Express **23**(7), 9130–9136 (2015).
24. C. Kim, E. C. Cho, J. Chen, K. H. Song, L. Au, C. Favazza, Q. Zhang, C. M. Cobley, F. Gao, Y. Xia, and L. V. Wang, "In vivo molecular photoacoustic tomography of melanomas targeted by bioconjugated gold nanocages," ACS Nano **4**(8), 4559–4564 (2010).
25. J. T. Oh, M. L. Li, H. F. Zhang, K. Maslov, G. Stoica, and L. V. Wang, "Three-dimensional imaging of skin melanoma in vivo by dual-wavelength photoacoustic microscopy," J. Biomed. Opt. **11**(3), 034032 (2006).
26. H. F. Zhang, K. Maslov, G. Stoica, and L. V. Wang, "Functional photoacoustic microscopy for high-resolution and noninvasive in vivo imaging," Nat. Biotechnol. **24**(7), 848–851 (2006).
27. "American national standard for the safe use of lasers," ANSI Standard Z136.1–2007 (2007).
28. O. Catalano, C. Caracò, N. Mozzillo, and A. Siani, "Locoregional spread of cutaneous melanoma: sonography findings," AJR Am. J. Roentgenol. **194**(3), 735–745 (2010).

1. Introduction

Melanoma, which develops from melanocytes, is the least common but the most lethal form of skin cancer [1].The incidence has significantly increased in the past 20 years [2]. Clinical decision-making and prognosis are depending on the stage of melanoma. With the development of tumor stage, fatality rate increased accordingly [3, 4]. Tumor thickness and tumor-associated vasculature are two key parameters for staging melanoma. Melanoma, based on its thickness, can be classified into four stages in the tumor–node–metastasis staging system, T1 (≤1.0 mm), T2 (1.01–2.0 mm), T3 (2.01–4.0 mm), and T4 (>4.0 mm) [5, 6]. Early recognition of melanoma is essential in the treatment of this cancer, for surgical margin of melanoma is determined by the staging system [7, 8]. Tumor-associated vasculature plays a pivotal role in the growth and metastasis of tumors because it not only regulates the supply of nutrients and oxygen to the tumor but also expedites tumor invasion and metastasis [9]. As an essential indicator of disease progression, vascularization level in tumor is used to assess the potential of metastatic tumor [9, 10]. Therefore, imaging the proliferation of tumor vasculature and measuring the thickness of melanoma are equally important for the diagnosis and prognosis of melanoma. Current clinical practice is based on incisional biopsy mostly. However, biopsy usually accompanies with pain and will damage to surrounding healthy

#253727 Received 12 Nov 2015; revised 14 Dec 2015; accepted 15 Dec 2015; published 5 Jan 2016

tissue. Therefore, a noninvasive biopsy method is urgently required for clinical practice of melanoma.

Several efforts were made to the noninvasive detection of melanoma, such as dermoscopy, sonography and photoacoustic imaging (PAI). In trained hands, dermoscopy was used to evaluate the characteristics of pigmented lesions of melanoma, since only ballistic regime can be imaged, the measurement of the thickness of melanoma was confined [11]. With good penetration depth, sonography was demonstrated to be a useful tool in the preoperative detection of thickness of malignant melanoma [12–15]. However, the examination accuracy rate is low in the detection of early-stage melanoma because of the poor definition at shallow levels [16, 17]. PAI was a hybrid imaging modality [18–21], the image can be reconstructed by detecting the acoustic pressure irradiated by a short pulsed laser beam [22–24]. Previous works demonstrated that PAI could be used in the detection of melanoma [25, 26], but melanin in most melanomas has a broad and strong absorption spectrum, which causes a high light attenuation. Consequently, PAI only showed great advantages in the detecting of early-stage melanoma.

In this study, an integrated photoacoustic (PA) and ultrasound (US) imaging system is developed. PA image contrast, which is derived from the absorption of chromophores, such as hemoglobin and melanin, provides a high optical contrast for tumor vasculature and early-stage melanoma. US image contrast, which originates from the differences in acoustic impedance, provides deeper image range for the thickness detection of late-stage melanoma, the skin layer could be clearly distinguished at the same time. An integrated detector with sound-light coaxial/confocal design and novel coupling mode is employed for dual-imaging strategy. These advantages of the integrated PA and US imaging strategy enable a holistic evaluation of melanoma, which dedicated to the *in vivo* biopsy of melanoma.

2. Methods and materials

The schematic of the experimental setup is shown in Fig. 1(a). A miniature laser (Horus Laser, France, HLX -I-F005), which operates at a wavelength of 532 nm with a pulse width of 1 ns and a repetition rate up to 5 KHz, is used as the excitation light source for PA imaging system. The output laser beam is collimated and then coupled into a single-mode fiber. The laser is focused on the sample with an objective. To conform to the American National Standards Institute safety limit (20 mJ/cm^2) [27], we limit the incident light energy density on the tissue surface to 15 mJ/cm^2. For US imaging system, an ultrasonic pulser/receiver (5073PR, Olympus) is employed to provide electrical pulse to the transducer. Devices in the blue dashed box are mounted on a scanning stage. The entire system is synchronized with the trigger provided by the laser system. A delay generator is also used to delay the ultrasound pulse for US imaging, thus allowing the desired temporal separation between PA and US signals [Fig. 1(b)]. The time delay is constant (30 μs) between each of the laser and ultrasound pulses. Therefore, the system can obtain PA and US signals from the same spatial location of the sample. It takes about 12 minutes to image a 10×10 mm^2 area with a laser repetition rate of 5 KHz.

Figure 1(c) shows the structure diagram and photo of the integrated detector, which consists of an objective (RMS4X, Thorlabs) and a focused ultrasound transducer (29 MHz center frequency, 80% −6dB bandwidth). A hole with 2 mm diameter is punched in the transducer center to pass through the optical illumination beam. There is a cover glass stick on the top surface of the hole, in order to prevent the objective stained by water. A conical coupling slot with double-layer structure is designed for coupling ultrasonic signals. The bottom of the coupling slot is truncated and sealed with a layer of polyethylene membrane for optical and acoustic transmission. The polyethylene membrane is clamped between two layers. The coupling slot is filled with water to ensure the transducer can submerge in water when tilted. The detector and objective lens is designed to be coaxial, so that optical and acoustic foci are aligned for co-localization scanning. Considering the refraction of water, the working

#253727 Received 12 Nov 2015; revised 14 Dec 2015; accepted 15 Dec 2015; published 5 Jan 2016

distance of objective is calculated to be 21 mm. The objective and transducer are connected with a fine-tuning threading adapter. The optical foci is 0.2 mm below the polyethylene membrane, which could be fine-tuned by a threading adapter. The imaging sensitivity has been improved from two aspects of design. First, by using a focused transducer, the detecting sensitivity has been greatly improved. Second, the optical and acoustic foci are designed aligned to maximize the detection sensitivity. Several advantages of the integrated detector are summarized. First, the coupling mode provides flexible detection rotational angle to accommodate different check positions. Second, optical and acoustic foci is designed to align, greatly facilitates the operation of doctors. Third, the polyethylene membrane in contact with the patient's skin can be replaced, to prevent cross infection effectively. This novel design makes the integrated detector be conveniently used in the clinical tests.

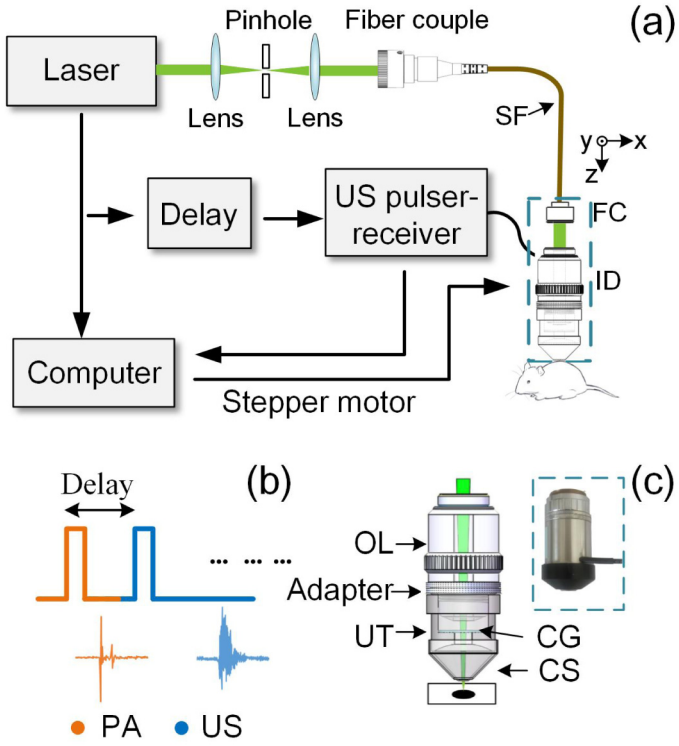

Fig. 1. Schematic of the PA and US dual-modality imaging system. (a) Experimental setup. SF: single-mode fiber; FC: fiber collimator; ID: integrated detector. (b) Timing diagrams for the trigger. (c) Structure diagram and photo of the integrated detector. OL: objective lens; UT: ultrasound transducer; CG: cover glass; CS: coupling slot.

3. Results

3.1 Resolution of the PA/US melanoma imaging system

Lateral and axial resolution experiments were performed to verify the imaging capability of the integrated system. The lateral resolution of the dual-modality imaging system is determined by the optical focus point. The numerical aperture (NA) of the objective lens with 4 × magnification is 0.1. The theoretical lateral resolution is estimated to be 2.7 μm at 532 nm by the formula 0.51 λ/NA. Figure 2(b) showed a maximum amplitude projection (MAP) PA image of the optical resolution chart. The scanning step of the system was set as 3 μm. The width of a bar and the space between two bars in the test target were 5 μm. Each bar can be clearly distinguished by PA image and agreed well with the test target. Figure 2(c) presented

#253727 Received 12 Nov 2015; revised 14 Dec 2015; accepted 15 Dec 2015; published 5 Jan 2016

the distribution of PA normalized function value along the dashed line in Fig. 2(b). The full-width at high magnitude of the line spread function was 3.5 μm, which was slightly larger than the theoretical value. Compared with US imaging, which provided a lateral resolution of 300 μm, PA image has demonstrated a better capability of microvascular imaging. The axial resolution, which is determined by time-resolved ultrasonic detection, can be estimated with the following formula: 0.88 c/B, where c is the sound speed of water (1500 m/s), and B is the ultrasonic transducer bandwidth. The theoretical value for the transducer used in our experiments is 57 μm. A sample that could provide a continuously variable distance was constructed to measure the axial resolution. As shown in Fig. 2(d), the sample was made up of two layers of red ink. One was on a polymethylpentene plastic, and the other was on a glass slide. The PA image of the sample was shown in Fig. 2(e). Figure 2(f) was the reconstructed profile of the sample marked by the white dotted line in Fig. 2(e). The axial resolution of the profile was estimated to be 60 μm, which matched well with the theoretical resolution.

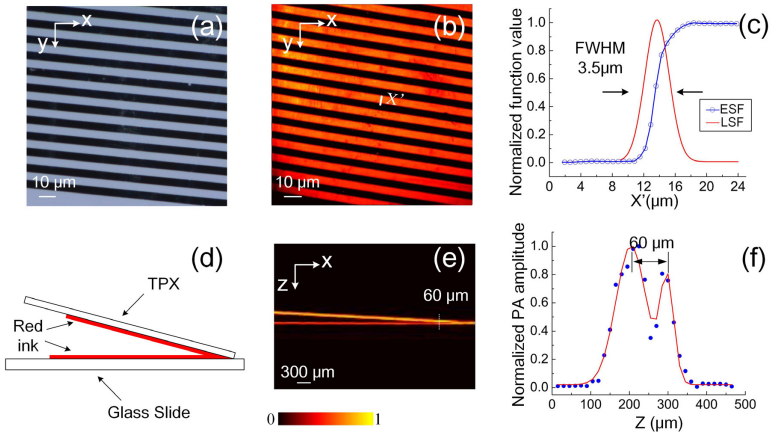

Fig. 2. Resolution of the dual-modality system. (a) Photograph of the optical resolution chart. (b) MAP image of the optical resolution chart. (c) Distribution of PA normalized function value along the dashed line in (b). ESF: edge spread function; LSF: line spread function. (d) Sample schematic of axial resolution. (e) PA B-scan image of the sample. (f) Normalized PA amplitude along the dashed line in (e).

3.2 Measuring the thickness of melanoma phantom by PA/US imaging

Phantom experiment was performed to demonstrate the capability of the PA/US imaging system in measuring the thickness of melanoma. Figure 3(a) showed the photograph of the phantom. Phantom sample of melanoma was consisted of three layers. Each layer was approximately 1.5 mm. The melanoma phantom was made of a mixture of black ink and gelatin, and the absorption coefficients were 170 cm^{-1}, which was close to the melanin pigmented tissues at 532 nm [28]. The background was made of gelatin, latex microspheres (polystyrene) and an intralipid mixture, which had similar optical characteristic and acoustic scattering coefficient with skin tissue. Figure 3(b) showed the cross-sectional (B-scan) PA image of the melanoma phantom. The same region of the melanoma phantom was enlarged and showed in the dotted box of PA image and US image [Fig. 3(c)]. Significantly, we get more detailed information about shallow layer of melanoma phantom from PA image than US image. However, the maximum imaging depth of PA image was not enough for showing the entire structure of the sample. US images showed the bottom of the mimic tissue with a high signal-to-noise ratio (SNR) complementary. In addition, US images also suggest the presence of the surface of the mimic tissue with a high signal-to-noise ratio (SNR). The thickness of melanoma phantom (4.5 mm) could be extracted by the combination of PA and US images in Fig. 3(d).

#253727 Received 12 Nov 2015; revised 14 Dec 2015; accepted 15 Dec 2015; published 5 Jan 2016

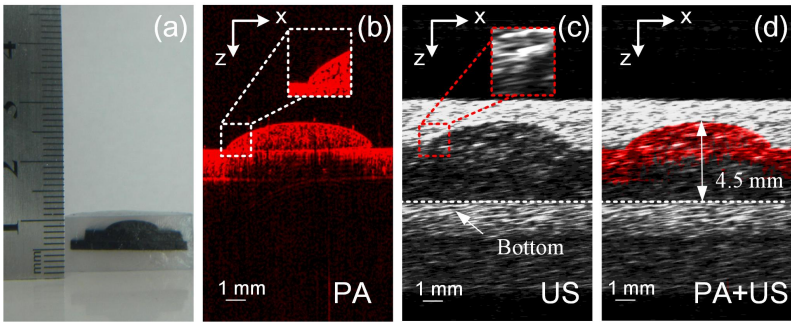

Fig. 3. Phantom imaging of the dual-modality system. (a) Photograph of melanoma phantoms. PA (b), US (c), and combined PA/US (d) images of the melanoma phantoms.

3.3 In vivo imaging of melanoma and surrounding vascular distribution in mice

To further demonstrate the capability of the dual-modality imaging system, we used it to *in vivo* investigate the development of subcutaneous melanoma and its surrounding vascular in mice. The melanoma mode was injected with Melanoma B16 cells subcutaneously on the dorsal side of mice (body weight: 20 g). Before the experiment, hair was removed from the back with a commercial hair remover (Payven Depilatory China). Sodium pentobarbital (40 mg/kg; supplemental, 10 mg/kg/h) was administered to keep the mice motionless during the experiment. The melanoma mice mode was examined twice separately at day 7 and 30 after the cell injection. After the second PA/US imaging, the mice was euthanatized, and the melanoma tissue was excised and stained with hematoxylin and eosin (H&E). All experimental animal procedures were carried out in accordance with the guidelines of the South China Normal University.

Figure 4(a) and Fig. 4(f) showed the *in vivo* PA MAPs of the melanoma in mice at different times (day 7 and 30 after cell injection). As shown in Fig. 4(a) and Fig. 4(f), the lateral resolution for *in vivo* tests was lower than simulation experiments, which was influenced by the dorsal skin of mice. Even though, the blood vessels around the tumor could still be clearly imaged by PA. Figure 4(b) and Fig. 4(g) were PA B-scan images obtained along the dotted lines shown in Fig. 4(a) and Fig. 4(f), respectively. Quantification of the number of vessels was obtained by MAPs of PA image first, some blood vessels with larger diameter can be counted directly, as indicated by the arrows 1, 2. Several capillaries which were confused from the MAPs, can be identified with the analysis of B-scan images, such as arrows 3′, 4’. The vessel number was counted by five volunteers respectively. Based on the PA images, we could clearly see the development of the microvasculature around the melanoma. At the same field of view, the vessel number increase from 9 ± 2 (day 7), to 14 ± 3 vessels (day 30). For the B-scan image, the thickness of melanoma could be determined by the time-domain waveform, and the sound speed was 1540 m/s (soft tissue). By contrast, PA image [Fig. 4(b)] of the thin melanoma (~420 μm) suggested a higher contrast than that of US image [Fig. 4(c)]. While the light with a high attenuation cannot easily penetrate the melanin-rich tumor, US image can compensate for the imaging depth. Melanoma visualized by US images was hypoechoic with a homogeneous echostructure, which indicated a maximal tumor thickness of 2.58 mm [Fig. 4(h)]. As shown in Fig. 4(j), the largest tumor thickness measured by H&E was 2.51 mm, which agreed well with the thickness measured by our system. The US and PA data sets was overlaid respectively to create compound display [Fig. 4(d) and 4(g)], mixed image showed the overall structure characteristics of melanoma: skin, blood vessels, acoustic impedance of tissue and thickness of melanoma for different stage. The quantitative results achieved by PA/US images exactly identify the development of melanoma.

#253727 Received 12 Nov 2015; revised 14 Dec 2015; accepted 15 Dec 2015; published 5 Jan 2016

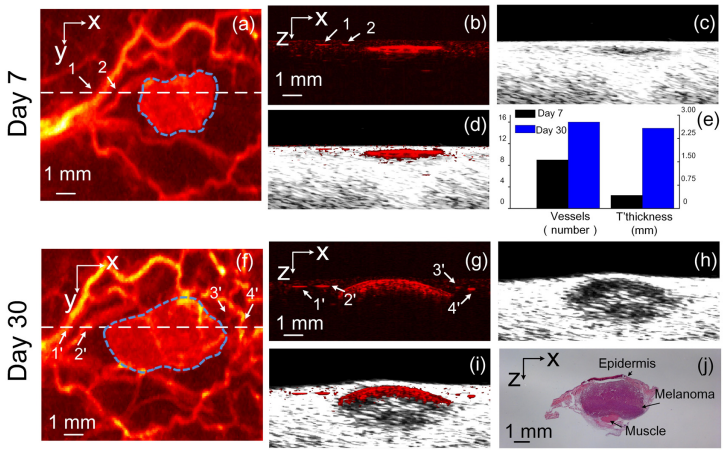

Fig. 4. MAP images of PA for day 7 (a) and day 30 (f). B-scan images of PA (b, g), US (c, h), and combined image (d, i) for the dot lines in (a) and (f). Quantitative statistics of the number of vessels and the maximum thickness of the melanoma (e). Histology image (H&E staining) (j).

4. Discussion

As shown in the Table 1, based on the PA/US imaging, several potential parameters for evaluating melanoma were extracted and compared with single imaging mode. This comparison demonstrated the limitation of single PA or US imaging modality in the detection of melanoma. US image provided high SNR for the detection of epidermis, which was utilized to ensure the depth of melanoma. However, it was weak to detect blood vessels and early stage of melanoma. PA imaging provided high resolution and high contrast images for the early stage melanoma and surrounding blood vessels. But limited imaging depth of PA restrict the ability of detecting the bottom boundary of thick melanoma.

Tab. 1. Average SNR of skin, the top/bottom boundary of melanoma at day 7 and day 30, blood vessels calculated from Fig. 4. (-, SNR is too weak to statistics)

Mode	Skin	Top boundary of melanoma (day 7)	Bottom boundary of melanoma (day 7)	Top boundary of melanoma (day 30)	Bottom boundary of melanoma (day 30)	Blood vessels
PA	-	~16 dB	~12 dB	~17 dB	-	~19 dB
US	~45 dB	-	-	~21 dB	~14 dB	-
PA + US	Clearly defined	Clearly defined	Defined	Clearly defined	Defined	Clearly defined

Despite the superiorities, several problems remain to be solved. First, since melanoma was confused with nevus in clinical screening frequently, and misdiagnosis result in serious medical consequences. US image contrast which was originated from the differences in acoustic impedance, provided a potential to distinguish melanoma from nevus. Following experiment will be designed to confirm this view. Second, the platform was not lightweight enough to be used in the clinical detection. Therefore, a miniature ultrasonic motor with high working speed will be employed in our future work for handheld design.

In summary, we developed an integrated PA and US imaging modality to visualize the multiple features of melanoma with a novel integrated detector. Simultaneous imaging of the proliferation of tumor vasculature and measuring the thickness of melanoma at different stages, encourage further development toward the *in vivo* biopsy of melanoma.

#253727 Received 12 Nov 2015; revised 14 Dec 2015; accepted 15 Dec 2015; published 5 Jan 2016

Acknowledgments

This research is supported by the National High Technology Research and Development Program of China (2015AA020901), the National Natural Science Foundation of China (61331001, 61361160414, 91539127), the Science and Technology Planning Project of Guangdong Province (2013B090500122, 2014A020215031), the Guangdong Natural Science Foundation (S2013020012646), and the Science and Technology Planning Project of Guangzhou, China (201508020112).

#253727 Received 12 Nov 2015; revised 14 Dec 2015; accepted 15 Dec 2015; published 5 Jan 2016